

# A hybrid approach for simulating turbulent collisions of hydrodynamically-interacting particles

Orlando Ayala <sup>a</sup>, Wojciech W. Grabowski <sup>b</sup>, Lian-Ping Wang <sup>a,\*</sup>

<sup>a</sup> *Department of Mechanical Engineering, University of Delaware, Newark, DE 19716, USA*

<sup>b</sup> *Mesoscale and Microscale Meteorology Division, National Center for Atmospheric Research, P.O. Box 3000, Boulder, CO 80307-3000, USA*

Received 24 January 2006; received in revised form 12 November 2006; accepted 15 November 2006  
Available online 8 January 2007

---

## Abstract

A hybrid direct numerical simulation (DNS) approach is proposed for simulating turbulent collisions of hydrodynamically-interacting particles, under the assumptions that the disturbance flows due to particles are very localized in space and there is a sufficient length-scale separation between the particle size and the Kolmogorov scale of the undisturbed turbulent flow. The approach consists of direct simulation of the undisturbed turbulent flow and an analytical representation of local small-scale disturbance flows induced by the particles. This hybrid DNS approach provides, for the first time, a quantitative research tool to study the combined effects of turbulence and hydrodynamic interactions on the motion and collisional interactions of small particles. Several numerical implementation issues are discussed, along with consistency and accuracy of the approach. Areas for further development of the approach are indicated.

© 2006 Elsevier Inc. All rights reserved.

*PACS:* 02.60.Cb; 45.50.Tn; 47.27.ek; 47.55.Kf; 92.60.Jq

*Keywords:* Hydrodynamic interaction; Particle-laden flow; Direct numerical simulation; Collision efficiency; Turbulence

---

## 1. Introduction

The collision-coalescence of small particles and droplets moving under the influence of gravity in a turbulent gas is of importance to a wide variety of applications in engineering and a host of phenomena in nature. Examples include production of particles through gas-phase reactions, combustion sprays, motion of cloud droplets in the atmosphere [1], and transport of aerosols and pollutants [2]. In these applications, particles are usually suspended in a turbulent gas. Most previous studies of particle or droplet coagulation in turbulent flows focus on the motion of individual small particles in response to the carrier-fluid turbulence [3–5]. Collision rates are given in terms of the geometric collision kernel ignoring short-range hydrodynamic (or

---

\* Corresponding author. Tel.: +1 302 831 8160; fax: +1 302 831 3619.  
E-mail address: [lwang@me.udel.edu](mailto:lwang@me.udel.edu) (L.-P. Wang).

aerodynamic) interactions. The main factors considered in geometric collisions are the local concentration of particles, the local turbulent velocity gradient and acceleration, and the relative settling velocity of particles if their sizes differ. Particle inertia leads to a local clustering of particles in response to the vortical structure of the turbulence, which is characterized by a radial distribution function of the particles [3,4]. The present work attempts to extend the previous studies to include the small-scale disturbance flows that each particle creates relative to the surrounding larger scale turbulence. This hydrodynamic interaction affects the efficiency of the collision process [6] as well as possible co-operative effects in enhancing the settling rates of particles [7].

If the growth of particles by the collision-coalescence process is of the central concern, the local hydrodynamic (or aerodynamic) interactions of particles must be considered even in a dilute turbulent suspension. In this type of systems, a unique *three-way coupling* occurs: (a) the carrier-flow turbulence affects the motion of the particles through the interfacial viscous drag; (b) the motion of each particle can be affected by the presence of other particles in the system, either through the strong local near-field binary hydrodynamic interaction or by the cumulative many-body, long-range interactions; and (c) the background carrier-fluid turbulence can also affect the hydrodynamic interactions as the turbulence defines both the far-field conditions and the local environment for the hydrodynamic interactions. In this paper, the terms particles and droplets are used interchangeably, so are the terms hydrodynamic interaction and aerodynamic interaction.

In such three-way coupling systems, the central issue is the relative importance of turbulent mixing of the particles versus the hydrodynamic interactions of particles in a random suspension. The dynamics of random suspensions in Stokes flow has been studied for some time and there is an extensive literature [8–14]. Suspensions of small solid particles in a gas where fluid inertia is negligible but particle inertia is considered have been studied by Kumaran and Koch [15,16]. Coagulation of two small solid particles in a simulated local random linear flow under hydrodynamic interactions and van der Waals attraction was considered in Brunk et al. [17]. The situation when both the hydrodynamic interactions of many particles and the background turbulence must be simultaneously considered is the subject of this paper, and currently, to the best knowledge of the authors, there is no rigorous theoretical and computational treatment of such systems. This paper reports a first step toward developing a rigorous computational approach for a three-way coupling system.

The motivation for this study is the need to understand and quantify the effect of air turbulence on the collision rates of droplets in atmospheric warm clouds [6]. The topic has received much attention in recent years (see reviews by Pinsky and Khain [18], Vaillancourt and Yau [19], Shaw [20]). In warm clouds, the mass loading ratio is on the order of  $10^{-3}$  or less, and the size of cloud droplets (5–50  $\mu\text{m}$ ) is typically one to two orders of magnitude smaller than the Kolmogorov scale ( $\sim 1$  mm) of the air turbulence; the effect of the droplets on the airflow momentum can be safely neglected. We must note that there could still be a significant energy coupling between the dispersed phase and the carrier fluid if the net rate of condensation or evaporation of water content is large enough to cause a significant latent heat release. A related issue is the entrainment of cold dry air into the cloudy air [20]. In this research, we treat the airflow as nearly adiabatic and inter-phase energy coupling is not considered. The hydrodynamic interactions must be considered as we are concerned with the growth of droplets caused by collision-coalescence. Therefore, while we assume one-way coupling at the scale of undisturbed carrier flow ( $>1$  mm), we do consider all couplings at the scale of droplet diameter ( $<0.1$  mm). An underlying assumption is that the undisturbed or background turbulence is decoupled from the disturbance flows due to the separation in length scales of the two types of flow fields. We note, however, that the disturbance flows are strongly affected by the background turbulence.

This special situation in the atmospheric clouds makes it possible to treat the undisturbed carrier-fluid turbulence and the disturbance flows separately. In most engineering applications, however, the particle size could be on the same order or larger than the Kolmogorov length scale of the undisturbed carrier flow. Obviously, the often used point-particle or point-force representation for the dispersed phase is no longer valid. In recent years, several groups have made efforts to simulate the particle motion and flow modulation for a turbulent suspension of finite-size particles, including the Stokesian-flow approach of Pan and Banerjee [21], the virtual-boundary forcing method of Pan and Banerjee [22], the force coupling method of Maxey and Patel [23] and Dance and Maxey [24], the semi-analytical method of Prosperetti and Oguz [25] and Takagi et al. [26], the field-coupling scheme of Tsuji et al. [27]. Other methods such as the body-fitted finite-element method and the Lattice Boltzmann method may also have the potential to be used for turbulent disperse flow with finite-size

particles, but so far they have mainly been used for suspension flows without carrier-fluid turbulence [28–31]. A noticeable exception is the study of particle collision in a liquid-solid turbulent flow using the Lattice Boltzmann method by Ten Cate et al. [32].

With the assumptions mentioned above, we shall introduce a hybrid approach that is similar in concept to the superposition method often used to model collision efficiency in cloud microphysics [33–37]. In traditional superposition method, the disturbance flow of each particle is unaffected by the presence of other particles, causing a poor representation of the no-slip boundary condition on the surface of each particle when two particles are nearby each other. Recently, Wang et al. [38] proposed improved formulations of the superposition method and tested them for the special case of a quiescent carrier fluid. They improved the accuracy of the superposition method by making an explicit use of the no-slip boundary conditions on the surface of each droplet.

In this paper, we extend the method of Wang et al. [38] to a turbulent carrier flow. This hybrid approach solves the turbulent flow by the pseudo-spectral method [44] with a large-scale forcing, and utilizes the improved superposition method to embed analytically the local, small-scale (10  $\mu\text{m}$  to 1 mm) disturbance flows induced by the particles. This hybrid representation is then used to study the combined effects of hydrodynamic interactions and airflow turbulence on the motion and collisions of cloud droplets. The hybrid approach should be viewed as a first step as far as the treatment of local hydrodynamic interactions is concerned. More rigorous treatments in the suspension mechanics such as the Stokesian dynamics [39] and other improved multipole methods [40–43] are appropriate if more accuracy is desired. Keeping the treatment of hydrodynamic interactions simple at this stage helps with the computational efficiency of the approach.

The paper is organized as follows. The method is described in Section 2. In Section 3, important implementation issues are discussed. Numerical accuracy and sensitivity are studied briefly in Section 4. Computational tests and results are presented in Section 5. Finally, in Section 6, we present main conclusions and indicate areas for further development.

## 2. Problem formulation and the hybrid approach

In this section, we shall briefly describe the cloud physics problem to lay the basis for the hybrid approach and to shed lights on the challenges that must be addressed by the approach. Then an approximate representation is developed to formulate the hybrid direct numerical simulation (DNS) approach.

### 2.1. Physical description

For the problem of droplets moving in a turbulent cloud, the droplets can be considered as a system of heavy particles carried by a turbulent airflow field  $\mathbf{U}(\mathbf{x}, t)$ . Typical droplet volume fractions are on the order of  $O(10^{-6})$  and mass-loading on the order of  $10^{-3}$ . Therefore, while the flow can affect the motion of droplets, the undisturbed air turbulence is not affected by the presence of the droplets (one-way coupling). The droplet size is typically one to two orders of magnitude smaller than the smallest length scale of the turbulence (the Kolmogorov length scale,  $\eta$ ). In a stagnant fluid, the disturbed flow due to a droplet could extend up to a region about 50 times the droplet radius [36,45]. This length is on the order of the Kolmogorov length scale of the airflow turbulence or less.

The particle Reynolds number is on the order of 0.01–1.0. As a first step towards the modeling of hydrodynamic interactions, the disturbance flow will be assumed to be a Stokes flow. For the special case of a droplet settling in a stagnant air at steady state with terminal velocity  $(0, 0, -v_p)$  (see Fig. 1), the disturbance flow can be written as

$$u_r = \left[ \frac{3}{2} \frac{a}{r} - \frac{1}{2} \left( \frac{a}{r} \right)^3 \right] v_p \cos \theta, \quad u_\theta = \left[ \frac{3}{4} \frac{a}{r} + \frac{1}{4} \left( \frac{a}{r} \right)^3 \right] (-v_p \sin \theta), \quad u_\phi = 0. \quad (1)$$

The local dissipation rate ( $\epsilon = 2\mu s_{ij}s_{ij}$ ) of this flow is

$$\epsilon(r, \theta) = \frac{\mu v_p^2}{r^2} \left( \frac{3}{2} \right)^2 \left\{ \cos^2 \theta \left[ 3 \left( \frac{a}{r} \right)^2 - 6 \left( \frac{a}{r} \right)^4 + 2 \left( \frac{a}{r} \right)^6 \right] + \left( \frac{a}{r} \right)^6 \right\}. \quad (2)$$

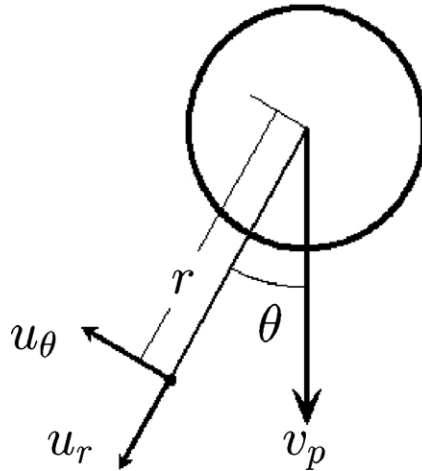


Fig. 1. A droplet settling at steady state with terminal velocity  $(0, 0, -v_p)$  in a stagnant fluid.

The total viscous dissipation  $F(r)$  contained within a spherical region of radius  $r$  from the center of the droplet is then

$$F(r) = \int_{r=a}^r \int_{\theta=0}^{\theta=\pi} \epsilon(r, \theta) 2\pi r^2 \sin \theta d\theta dr = \left\{ 1 - \frac{1}{2} \left[ 3 \left( \frac{a}{r} \right) - 2 \left( \frac{a}{r} \right)^3 + \left( \frac{a}{r} \right)^5 \right] \right\} 6\pi\mu a v_p^2. \quad (3)$$

The total viscous dissipation  $F(r \rightarrow \infty)$  in the disturbance flow around the droplet is equal to  $6\pi\mu a v_p^2$ , which is equal to the rate of loss of potential energy of the droplet ( $m_p |\mathbf{g}| v_p$ ). Here,  $v_p$  is the single-droplet terminal velocity,  $\mu$  is the air viscosity,  $a$  is the radius of the droplet,  $m_p$  is the mass of the droplet, and  $\mathbf{g}$  is the gravitational acceleration. Fig. 2 shows how  $F(r)$  changes with  $r$ . The region  $r/a \leq 10$  contains 85% of the total viscous dissipation of the disturbance flow. Therefore, the kinetic energy introduced into the fluid by the disturbance flow converts to viscous dissipation locally and quickly. Since the droplets are much smaller than the Kolmogorov eddy, the disturbance flow is contained within a turbulent energy-dissipation eddy.

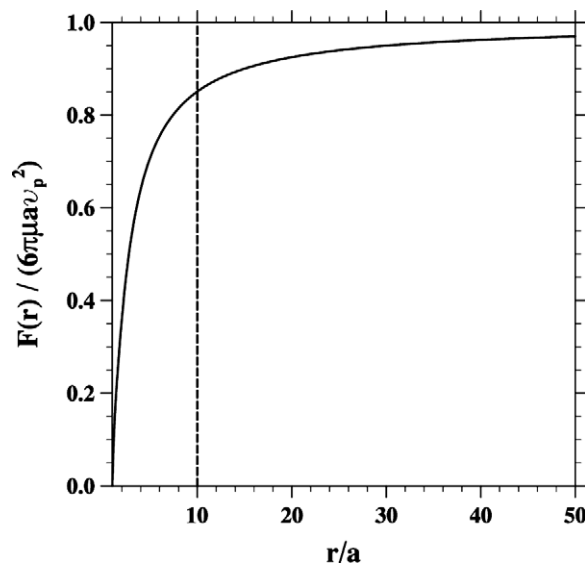


Fig. 2. The distribution of normalized viscous dissipation in the disturbance flow.

This discussion illustrates why the point-force technique is a reasonable approximation for very small particles in a turbulent flow. In our application, although the disturbance flow does not affect the background turbulent flow, if another droplet reaches into the disturbance flow region, its motion will be affected by the disturbance flow (i.e., local hydrodynamic interaction). In the following section, we present a numerical approach that can capture the hydrodynamic interactions due to the disturbance flows embedded in a background air turbulence.

### 2.2. The hybrid approach

The background air turbulence  $\mathbf{U}(\mathbf{x}, t)$  is simulated by solving the Navier–Stokes equation directly. Fig. 3 compares the particle size and inter-particle spacing with the grid spacing of the DNS of the background turbulent flow field. A large number ( $N_p$ ) of small particles are introduced into the computational domain, with velocities  $\mathbf{V}^{(k)}(t)$  ( $k = 1, \dots, N_p$ ). The particle radius is typically  $0.0415\eta$  and the average particle–particle separation distance  $d_{\text{int}}$  is about  $3\eta$  for a particle volume fraction of  $10^{-6}$ . The above corresponds to droplets of  $24.5 \mu\text{m}$  radius in a turbulent flow with flow dissipation rate of  $400 \text{ cm}^2/\text{s}^3$  and a liquid water content of  $1 \text{ g}/\text{m}^3$ . It should be noted that in studies of droplet growth in a cumulus cloud, the dissipation rate could range from 1 to  $1000 \text{ cm}^2/\text{s}^3$ , the above specific flow dissipation rate is used to illustrate the relative scales of the problem. In engineering flows the dissipation rate could be higher.

In our pseudospectral DNS of the background turbulence, the grid spacing is typically twice the Kolmogorov length scale,  $\Delta x \sim 2\eta$ . Clearly, the disturbance flow field  $\tilde{\mathbf{u}}(\mathbf{x}, t)$  which may be thought as a superposition of the  $N_p$  very localized Stokes flows surrounding the  $N_p$  droplets. Therefore,  $\tilde{\mathbf{u}}(\mathbf{x}, t)$  depends on the locations of all  $N_p$  droplets and their relative motion to the turbulent fluid.

The flow field experienced by a droplet is then the combination of the undisturbed turbulent flow  $\mathbf{U}(\mathbf{x}, t)$  and the disturbance flow  $\tilde{\mathbf{u}}(\mathbf{x}, t)$  but with its own disturbance flow removed. The combined flow field,  $\tilde{\mathbf{U}}(\mathbf{x}, t) \equiv \mathbf{U}(\mathbf{x}, t) + \tilde{\mathbf{u}}(\mathbf{x}, t)$ , is referred to as the composite flow field. The key element here is the proper and optimum specification of  $\tilde{\mathbf{u}}(\mathbf{x}, t)$ , provided that  $\mathbf{U}(\mathbf{x}, t)$  is known.

Since the Stokes disturbance flows are each governed by the linear Stokes equation, they can be superimposed to still satisfy the same Stokes equation locally [38]. This is the physical basis of the superposition method [33,1]. The challenge is to satisfy the no-slip boundary conditions for all the particles in the system.

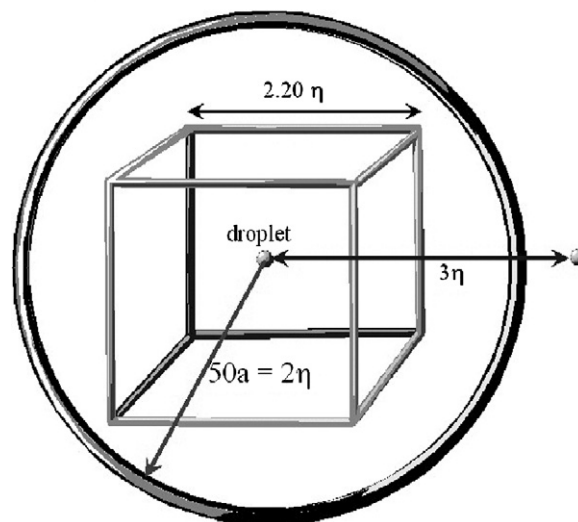


Fig. 3. Relative length scales in the hybrid DNS. The cube represents grid cell size in HDNS, the circle indicates domain of influence for hydrodynamic interactions. For  $64^3$  DNS at  $R_\lambda = 40$ , computational domain is about  $141\eta$ , grid cell size is about  $2.2\eta$ , particle diameter is  $0.083\eta$ , and the particle–particle separation distance is  $3\eta$ .

Wang et al. [38] recognized that, by optimizing the magnitude of the disturbance flow experienced by each particle, it is possible to satisfy the no-slip boundary condition on the surface of each particle when averaged over the surface of the particle. Specifically, the fluid velocity of the composite flow at the center of each particle is equal to the velocity of that particle. This requirement leads to a more accurate representation of the force acting on a particle due to the disturbance flows by all other particles than the original superposition method.

In a turbulent carrier flow, the disturbance flow field in a system containing  $N_p$  small particles can be written as

$$\tilde{\mathbf{u}}(\mathbf{x}, t) = \sum_{k=1}^{N_p} \mathbf{u}_s(\mathbf{r}^{(k)}; a^{(k)}, \mathbf{V}^{(k)} - \mathbf{U}(\mathbf{Y}^{(k)}, t) - \mathbf{u}^{(k)}), \quad (4)$$

where

$$\mathbf{u}_s(\mathbf{r}^{(k)}; a^{(k)}, \mathbf{V}_p^{(k)}) \equiv \left[ \frac{3}{4} \frac{a^{(k)}}{r^{(k)}} - \frac{3}{4} \left( \frac{a^{(k)}}{r^{(k)}} \right)^3 \right] \frac{\mathbf{r}^{(k)}}{(r^{(k)})^2} (\mathbf{V}_p^{(k)} \cdot \mathbf{r}^{(k)}) + \left[ \frac{3}{4} \frac{a^{(k)}}{r^{(k)}} + \frac{1}{4} \left( \frac{a^{(k)}}{r^{(k)}} \right)^3 \right] \mathbf{V}_p^{(k)} \quad (5)$$

represents the Stokes disturbance flow due to the  $k$ th droplet of radius  $a^{(k)}$  moving at velocity  $\mathbf{V}_p^{(k)}$  in an otherwise quiescent fluid, and  $\mathbf{r}^{(k)} \equiv \mathbf{x} - \mathbf{Y}^{(k)}$ . Here,  $\mathbf{Y}^{(k)}$  is the instantaneous location of the  $k$ th droplet. Eq. (5) is based on a single isolated particle and represents a combination of a Stokeslet and a potential dipole flow. In a multi-particle system the coefficients of each term could differ from those specified in Eq. (5). It may be desirable to include effects of local variations in the Stokes flow on the surface of the particle relative to the velocity at the center such as Faxen corrections. It would also be possible to include a force dipole (stresslet) [11] in the above formulation to extend the capability of the approach.

Eq. (4) contains explicitly the disturbance flow velocity  $\mathbf{u}^{(k)}$  at the location  $\mathbf{Y}^{(k)}$  of the  $k$ th droplet, due to all other droplets in the system. In Eq. (4), the combination  $[\mathbf{V}^{(k)} - \mathbf{U}(\mathbf{Y}^{(k)}, t) - \mathbf{u}^{(k)}]$  represents the relative velocity between the  $k$ th droplet and the composite flow  $\tilde{\mathbf{U}}(\mathbf{x}, t)$ , excluding the disturbance flow due to the  $k$ th droplet itself. Namely,  $\mathbf{u}^{(k)}$  represents the disturbance flow velocity due to all droplets except the  $k$ th droplet, at the location of the  $k$ th droplet.  $\mathbf{u}^{(k)}$  is determined by applying the center-point approximation [38] to the boundary conditions  $\tilde{\mathbf{U}}(|\mathbf{r}^{(k)}| = a^{(k)}, t) = \mathbf{V}^{(k)}$ , yielding

$$\mathbf{u}^{(k)} = \sum_{\substack{m=1 \\ m \neq k}}^{N_p} \mathbf{u}_s(\mathbf{d}^{(mk)}; a^{(m)}, \mathbf{V}^{(m)} - \mathbf{U}(\mathbf{Y}^{(m)}, t) - \mathbf{u}^{(m)}), \quad \text{for } k = 1, 2, \dots, N_p \quad (6)$$

where  $\mathbf{d}^{(mk)} \equiv \mathbf{Y}^{(k)} - \mathbf{Y}^{(m)}$ . Therefore,  $\mathbf{u}^{(k)}$  is a function of the background flow field and, the instantaneous locations and velocities of *all* particles. Eq. (6) implies that each disturbance flow velocity component at the location of the  $k$ th particle will depend on all the disturbance flow velocity components of all other particles. Eq. (6) is a large linear system of dimension  $3N_p$ . The drag force acting on the  $k$ th particle due to the interactions with the turbulent flow field and the disturbance flow field can be rigorously shown to be [38]

$$\mathbf{D}^{(k)}(t) = -6\pi\mu a_k [\mathbf{V}^{(k)}(t) - (\mathbf{U}(\mathbf{Y}^{(k)}(t), t) + \mathbf{u}^{(k)})]. \quad (7)$$

Therefore, the equation of motion of any given particle “ $k$ ” is

$$\frac{d\mathbf{V}^{(k)}(t)}{dt} = - \frac{\mathbf{V}^{(k)}(t) - (\mathbf{U}(\mathbf{Y}^{(k)}(t), t) + \mathbf{u}^{(k)})}{\tau_p^{(k)}} - \mathbf{g}, \quad (8)$$

$$\frac{d\mathbf{Y}^{(k)}(t)}{dt} = \mathbf{V}^{(k)}(t), \quad (9)$$

where  $\tau_p^{(k)} = 2\rho_p(a^{(k)})^2/(9\mu)$  is the particle inertial response time,  $\rho_p$  is the density of the particle, and  $\mu$  is the air dynamic viscosity. Without the disturbance flow, there are two important governing parameters for the motion of any particle [46]: the first is the Stokes number defined as  $St \equiv \tau_p/\tau_k$ , the ratio of particle response time to flow Kolmogorov time  $\tau_k$ ; the second is the nondimensional terminal velocity defined as  $S_v \equiv (\tau_p|\mathbf{g}|)/v_k$ , the ratio of particle terminal velocity to the flow Kolmogorov velocity  $v_k$ .

In both Eqs. (7) and (8), the disturbance flow velocity experienced by each particle,  $\mathbf{u}^{(k)}$ , plays the central role.

What we have formulated is a hybrid DNS approach in which the disturbance flow is represented analytically while the undisturbed turbulent flow is solved numerically using an accurate pseudospectral method. In this approach, the disturbance flows will incorporate naturally the droplet–droplet hydrodynamic interactions when droplets are in close proximity on the scale of droplet diameter. Details on the numerical implementation are described in the next section.

### 3. Numerical implementation

The implementation details of direct numerical simulation of dispersed turbulent flow without hydrodynamic interactions have been discussed extensively elsewhere in the literature [46,4,5], so only a brief description will be presented. The new dimension here is the treatment of particle-particle hydrodynamic interactions through the disturbance flow field. At each time step the following 5-step procedure was implemented:

- (1) Advance the undisturbed fluid turbulence field  $\mathbf{U}(\mathbf{x}, t)$  using a pseudo-spectral method.
- (2) Interpolate the undisturbed fluid velocities at the locations of the droplets,  $\mathbf{U}(\mathbf{Y}^{(k)}, t)$ .
- (3) Solve the disturbance flow velocity  $\mathbf{u}^{(k)}$  experienced by each droplet.
- (4) Advance the velocities and locations of the droplets.
- (5) Detect droplet–droplet collision events and calculate relevant kinematic and dynamic properties [6] as necessary.

#### 3.1. Background turbulent flow simulation

The turbulent flow is assumed to be homogeneous and isotropic, and solved by direct numerical simulations using a pseudo-spectral method. The incompressible, time-dependent, and three-dimensional Navier–Stokes equation

$$\frac{\partial \mathbf{U}}{\partial t} = \mathbf{U} \times \boldsymbol{\omega} - \nabla \left( \frac{P}{\rho} + \frac{1}{2} \mathbf{U}^2 \right) + \nu \nabla^2 \mathbf{U} + \mathbf{f}(\mathbf{x}, t), \quad (10)$$

was solved along with the continuity equation  $\nabla \cdot \mathbf{U} = 0$ . Here,  $\boldsymbol{\omega} \equiv \nabla \times \mathbf{U}$  is the flow vorticity,  $P$  is the pressure,  $\rho$  is the air density, and  $\nu$  is the air kinematic viscosity.

The flow was simulated in two stages. The first stage was to generate the flow from rest by the random forcing term  $\mathbf{f}(\mathbf{x}, t)$  which is nonzero only for a few modes at low wave numbers. We evolve the flow from  $t = 0$  to at least  $t = 9T_e$  ( $T_e$  is the large-eddy turnover time) to ensure it has reached a statistically stationary state. Such a flow state is characterized by a balance, on average, between the rate of energy introduced by  $\mathbf{f}(\mathbf{x}, t)$  and the rate of viscous energy dissipation. The small-scale features of the flow are characterized by the Kolmogorov scales defined based on the viscous dissipation rate and kinematic viscosity; namely, the Kolmogorov length, time, and velocity scale are

$$\eta = (\nu^3/\epsilon)^{1/4}; \quad \tau_k = (\nu/\epsilon)^{1/2}; \quad v_k = (\nu\epsilon)^{1/4}.$$

The large-scale features may be characterized by the r.m.s. fluctuation velocity or flow Taylor-microscale Reynolds number

$$u' \equiv \sqrt{\frac{\langle \mathbf{U} \cdot \mathbf{U} \rangle}{3}}, \quad R_\lambda = \sqrt{15} \left( \frac{u'}{v_k} \right)^2.$$

In the second stage, droplets were introduced into the flow and transported by the turbulence. At this stage, flow parameters were calculated and particle statistics were accumulated. Table 1 lists the flow parameters of a DNS turbulent airflow used throughout this work (from top to bottom): the Eulerian integral length scale  $L_e$ , the longitudinal Taylor microscale of fluid acceleration  $\lambda_D$  (see Hu and Mei [47]), and the variance of fluid acceleration  $\langle (D\mathbf{u}/Dt)^2 \rangle$ . The other derived flow properties are the transverse Taylor microscale length  $\lambda \equiv (15\nu u'/\epsilon)^{1/2}$ , the large-eddy turnover time  $T_e \equiv u'/\epsilon$ , and the integral length scale  $L_f \equiv u'T_e$ .

Table 1

Parameters and flow characteristics at  $\epsilon = 400 \text{ cm}^2/\text{s}^3$  and  $\nu = 0.17 \text{ cm}^2/\text{s}$ 

	<b>32<sup>3</sup></b>	<b>64<sup>3</sup></b>	<b>128<sup>3</sup></b>
	$u' = 7.05 \text{ cm/s}$ $R_\lambda = 23.37$	$u' = 9.57 \text{ cm/s}$ $R_\lambda = 43.04$	$u' = 12.42 \text{ cm/s}$ $R_\lambda = 72.41$
$L_e$ (cm)	0.884	1.372	2.440
$\lambda_D$ (cm)	0.2944	0.3361	0.3544
$\langle (D\mathbf{u}/Dt)^2 \rangle$ ( $\text{cm}^2/\text{s}^4$ )	$1.825 \times 10^4$	$3.002 \times 10^4$	$4.008 \times 10^4$
$\lambda$ (cm)	0.563	0.764	0.991
$T_e$ (s)	0.124	0.229	0.385
$L_f$ (cm)	0.884	2.206	4.837
Box size $L$ (cm)	4.192	8.384	16.768
$\Delta x$ (cm)	0.131	0.131	0.131
$dt_{\text{flow}} \times 10^3$ (s)	0.722	0.555	0.449

The Kolmogorov scales are:  $\eta = 0.0592 \text{ cm}$ ,  $\tau_k = 0.0206 \text{ s}$ ,  $v_k = 2.87 \text{ cm/s}$ .

We also present in the tables the size of the computational domain  $L$ , the grid spacing  $\Delta x$ , and the time step size for flow evolution  $dt_{\text{flow}}$ . The time step was chosen to ensure that the CFL number was 0.3 or less for numerical stability and accuracy. The spatial resolution of the simulations were monitored by the value  $k_{\text{max}}\eta$  which was always greater than unity to ensure that the smallest scales of flow are adequately resolved. Further details may be found in Wang and Maxey [46] and Wang et al. [4].

### 3.2. Undisturbed fluid velocities at the locations of droplets

In physical space, the undisturbed fluid velocities are readily available at the nodal points in DNS. Droplets are found anywhere in the computational domain. The fluid velocity at the location of every droplet  $\mathbf{U}(\mathbf{Y}^{(k)}, t)$  is interpolated from the values at neighboring grids points using a 6-point Lagrange interpolation in each direction [48]. The computational time for this part is proportional to the number of droplets followed in the simulation.

### 3.3. Disturbance flows and hydrodynamic interactions

The next step is to solve for the disturbance flow velocity experienced by each droplet,  $\mathbf{u}^{(k)}$ , from Eq. (6), before the position and velocity of each droplet can be advanced by Eqs. (8) and (9). Eq. (6) represents a linear system of  $3N_p$  unknown variables. This large linear system is solved iteratively by the Gauss–Seidel method [49]. To simplify the notation, we define  $\mathbf{U}^{(k)} \equiv \mathbf{U}(\mathbf{Y}^{(k)}, t)$ . Substituting Eq. (5) to Eq. (6), the system of equations can be rewritten in algebraic form as

$$u_i^{(k)} = \sum_{\substack{m=1 \\ m \neq k}}^{N_p} (A^{(mk)} d_i^{(mk)} \mathbf{d}^{(mk)} \cdot \mathbf{u}^{(m)} + B^{(mk)} u_i^{(m)}) + C_i^{(k)} \quad \text{for } i = 1, 2, 3 \text{ and } k = 1, 2, 3, \dots, N_p, \quad (11)$$

where  $u_i^{(k)}$  is the  $i$ th component of  $\mathbf{u}^{(k)}$ . Here,  $A^{(mk)}$ ,  $B^{(mk)}$ , and  $C_i^{(mk)}$  are defined as

$$\begin{aligned} A^{(mk)} &\equiv \left[ \frac{3}{4} \frac{a^{(m)}}{d^{(mk)}} - \frac{3}{4} \left( \frac{a^{(m)}}{d^{(mk)}} \right)^3 \right] \frac{1}{(d^{(mk)})^2} \\ B^{(mk)} &\equiv \left[ \frac{3}{4} \frac{a^{(m)}}{d^{(mk)}} + \frac{1}{4} \left( \frac{a^{(m)}}{d^{(mk)}} \right)^3 \right] \\ C_i^{(k)} &\equiv \sum_{\substack{m=1 \\ m \neq k}}^{N_p} \left\{ A^{(mk)} d_i^{(mk)} [(\mathbf{V}^{(m)} - \mathbf{U}^{(m)}) \cdot \mathbf{d}^{(mk)}] + B^{(mk)} (V_i^{(m)} - U_i^{(m)}) \right\}. \end{aligned} \quad (12)$$

The iterative procedure is implemented at the  $l$ th iteration as

$$u_i^{(k)l+1} = \sum_{m=1}^{k-1} (A^{(mk)} d_i^{(mk)} \mathbf{d}^{(mk)} \cdot \mathbf{u}^{(m)l+1} + B^{(mk)} u_i^{(m)l+1}) + \sum_{m=k+1}^{N_p} (A^{(mk)} d_i^{(mk)} \mathbf{d}^{(mk)} \cdot \mathbf{u}^{(m)l} + B^{(mk)} u_i^{(m)l}) + C_i^{(k)},$$

for  $i = 1, 2, 3$  and  $k = 1, 2, 3, \dots, N_p$ .

(13)

The solution is viewed to be converged if the following condition is met

$$\frac{|u_i^{(k)l+1} - u_i^{(k)l}|}{u_{\text{character}}} \leq \varepsilon,$$
(14)

where  $u_{\text{character}}$  is a characteristic velocity. For a monodisperse system with droplets settling under gravity, the gravitational settling velocity is used for  $u_{\text{character}}$ , while for a bidisperse system  $u_{\text{character}}$  is defined as the differential settling velocity ( $u_{\text{character}} = |v_{p2} - v_{p1}|$ ). When the turbulence has the strongest effect on the droplet motion, then  $u_{\text{character}}$  is set to the r.m.s. droplet velocity. The convergence criterion is applied to every disturbance velocity component for each particle. The tolerance parameter  $\varepsilon$  is determined by a combined consideration of numerical accuracy and computational efficiency. More details on  $\varepsilon$  are given in next sections.

Since the Stokes flow induced by the  $m$ th particle decays with  $\mathbf{d}^{(mk)}$  as  $d^{(m)}/d^{(mk)}$ , as an approximation and also for computational efficiency, we truncate the right hand side of Eq. (6) (therefore, Eq. (11)) at  $d^{(mk)}/a_m = H$ , or only contributions to the summation from neighboring particles with  $d^{(mk)}/a_m \leq H$  are considered. Physically, the dimensionless truncation radius  $H$  should be made on the order of  $(Re_p)^{-1}$  as the far-field disturbance flow can be better modelled by the Oseen's equation [11,50], where  $Re_p$  is the particle Reynolds number. The screening mechanism related to the fluid inertia [51–53] implies that, if the inter-particle separation is larger than the flow Kolmogorov scale, the flow Kolmogorov scale could also affect the truncation radius  $H$ . We speculate that, for a dilute turbulent suspension considered in our paper, the truncation radius will depend on both the particle size and the flow Kolmogorov scale, the exact nature of these dependences is a topic for future research. As a first step, in this study the truncation radius  $H$  is determined by a combined consideration of numerical accuracy and computational efficiency. We will discuss this point further in Section 4.2. The efficient cell-index method, with cell size equal to the truncation radius  $H \times \max(a_1, a_2)$ , and the concept of linked lists [54] are used here to quickly identify all the pairs participating in hydrodynamic interactions.

The simulation of a bidisperse system considered all hydrodynamic interactions (i.e., 1–1, 1–2, 2–2), where 1–1 denotes hydrodynamic interactions among size-1 particles, 1–2 denotes hydrodynamic interactions of size-1 particles with size-2 particles, and 2–2 hydrodynamic interactions among size-2 particles.

### 3.4. Motion of droplets

Once the background turbulent flow field  $\mathbf{U}(\mathbf{Y}^{(k)}, t)$  and the disturbance flow velocities  $\mathbf{u}^{(k)}$  have been solved, the velocities and locations of all droplets are advanced using Eqs. (8) and (9). A fourth-order Adams–Bashforth method was used to numerically integrate these two differential equations.

The droplets were introduced randomly into the computational domain when the background turbulent flow had reached the statistically stationary stage. The initial velocity condition was set equal to the local fluid velocity plus the terminal velocity of the droplet  $v_p$ . Collision-related statistics were accumulated to obtain running averages only after a time about  $3 \times \max(\tau_{p1}, \tau_{p2})$  in order to minimize any effect of the initial conditions.

The time step  $dt$  for advancing the droplet motion is chosen by a sensitivity analysis (see Section 4.1). The total number of droplets  $N_p$  in the simulation is estimated by the observed liquid water content in atmospheric clouds.

The numerical approach can be used to study simplified versions of the problem. When the hydrodynamic interaction velocities  $\mathbf{u}^{(k)}$  ( $k = 1, 2, \dots, N_p$ ) are set to zero, the geometric collision process can be studied. While if the gravity or the turbulent flow is not considered, then  $\mathbf{g}$  or  $\mathbf{U}(\mathbf{Y}^{(k)}, t)$  is set to zero.

### 3.5. Collision detection and kinematic statistics

This last step concerns numerical detection of collision events and related post-processing calculations. Collision detection was based on the efficient cell-index method and the concept of linked lists [54]. A collision detection grid was properly chosen so that all collision events were counted and, at the same time, no time was wasted on processing pairs of large separations. A collision event was counted during the time step if  $|\mathbf{r}(t)| \equiv |\mathbf{Y}^{(2)}(t) - \mathbf{Y}^{(1)}(t)|$  became less or equal to  $(a_1 + a_2)$ . In the current approach, the lubrication force at very small separations is underestimated so two particles can overlap, and when this occurs a coalescence event is assumed. While we were primarily interested in the 1–2 collision events, self collisions (1–1 and 2–2) were also detected.

No particles were allowed to overlap in space. Whenever two droplets collided, they were immediately removed from their current locations and, at the same time, two new droplets having the same material properties as the pair just removed were added back to the computational domain. The locations of the two new droplets were randomly chosen and care was taken to make sure that they did not overlap with any other droplets in the system. Their velocities were set to their terminal velocity plus the local fluid velocity. They were then tracked by solving their equation of motion just like all other droplets. In this manner, the total number of droplets remain the same and no droplet overlaps with any other droplets at the beginning of any time step. The above treatment mimics most closely the real situation of stochastic collision-coalescence of cloud droplets, since coalescence of two droplets will transform these droplets from their own size groups to a larger size group, while coalescence of smaller droplets can introduce new droplets to these size groups being considered.

A variety of statistics related to individual droplets and droplet-droplet interactions were computed. The statistics most relevant to our study were the mean velocities of droplets in all three directions for both sizes and the particle-particle radial relative velocity at contact. The pair statistics such as the radial distribution functions [3,5] were also considered. Further details on collision detections and computation of these statistical properties can be found in Wang et al. [4] and Zhou et al. [55,5].

## 4. Numerical accuracy and sensitivity

Several issues related to the computational efficiency and numerical accuracy of the hybrid DNS approach must now be discussed. These include the determination of the time step size  $dt$ , the truncation radius  $H$  for disturbance flows, and the tolerance parameter  $\epsilon$  for the Gauss–Seidel procedure. The first purpose of this section is to develop some general guidelines for selecting these implementation parameters in order to ensure that physical results will not be affected by these numerical details.

A separate issue is the statistical uncertainty of any computed quantity from this hybrid approach. The approach may be viewed as a controlled numerical experiment, in which a limited spatial domain is selected with a finite number of droplets in the system. Since the system is statistically homogeneous and stationary, averages over space, time and droplet pairs can be taken together to estimate and control the statistical errors. The second purpose of this section is to reveal the level of statistical uncertainty and its dependence on the number of droplets used in the simulation.

### 4.1. Time step size

Since a same time step  $dt$  was used to evolve the undisturbed turbulence, to advance the droplet motion, and to treat hydrodynamic and collisional interactions, the suitable value of  $dt$  must be determined to ensure that all these processes can be accurately represented in the numerical method. If  $dt_{\text{flow}}$  is the time step size needed to evolve the flow and  $dt_{\text{part}}$  is the time step size suitable for handling the droplet motion and collisional/hydrodynamic interactions, then  $dt$  can be chosen as  $dt = \min(dt_{\text{flow}}, dt_{\text{part}})$ .

The flow-evolution time step  $dt_{\text{flow}}$  for pseudospectral DNS is determined by making sure that the CFL number [56] is less than one for numerical stability. As a specific example, we consider the DNS turbulent flow at  $\epsilon = 400 \text{ cm}^2/\text{s}^3$  and resolution of  $64^3$ . In this case,  $dt_{\text{flow}} = 5.55 \times 10^{-3} \text{ s}$  provides a CFL of 0.28. The time step for the particle advancement,  $dt_{\text{part}}$ , should be a small fraction of the particle response time  $\tau_p$ . Wang et al.

[4] suggested that  $dt_{\text{part}} \leq 0.2\tau_p$  is appropriate when tracking motion of particles in a monodisperse system. This guideline can be extended to a bidisperse case by setting  $dt_{\text{part}} \leq 0.2 \min(\tau_{p_1}, \tau_{p_2})$ . However, the inclusion of particle hydrodynamic interactions may bring further restrictions to  $dt_{\text{part}}$ .

A sensitivity analysis is performed here to study the effect of time step size on the dynamic collision kernel  $\Gamma$  which is defined as

$$\Gamma = \frac{\dot{N}\Omega^2}{n_{\text{pairs}}}, \quad (15)$$

where  $n_{\text{pairs}}$  is the total number of distinct particle pairs,  $\dot{N}$  is the rate of collisions per unit volume, and  $\Omega$  is the volume of the computational domain. For a monodisperse system of  $N_p$  particles,  $n_{\text{pairs}} = N_p(N_p - 1)/2$ , while for a bidisperse system of  $N_{p_1}$  size-1 particles and  $N_{p_2}$  size-2 particles,  $n_{\text{pairs}} = N_{p_1}N_{p_2}$ .

We first selected a monodisperse case with  $St = 0.05$ ,  $Sv = 0.45$ ,  $a/\eta = 0.08$ , and  $N_p = 200,000$ , the results for five different values of  $dt_{\text{part}}$ , normalized by the value from the smallest  $dt$  case ( $dt = 0.05\tau_p$ ), are shown in Fig. 4a. The error bars indicate uncertainties corresponding to one standard deviation. Here,  $dt_{\text{flow}}$  was always larger than  $dt_{\text{part}}$ , thus  $dt = dt_{\text{part}}$ . The results for  $\Gamma$  appear to be independent of  $dt$  when  $dt \leq 0.15\tau_p$ . The upper limit  $0.15\tau_p$  is smaller than  $0.20\tau_p$  previously found for non-interacting particles, perhaps due to the hydrodynamic interactions causing the motion of a given particle to couple with the motion of all other particles in the system.

A bidisperse case with  $N_{p_1} = N_{p_2} = 100,000$ ,  $St_1 = 0.06341$ ,  $Sv_1 = 0.44656$ ,  $a_1/\eta = 0.01689$ ; and  $St_2 = 0.57067$ ,  $Sv_2 = 4.01904$ ,  $a_2/\eta = 0.05068$  was also chosen for the sensitivity study. This case corresponds to water droplets of 10  $\mu\text{m}$  and 30  $\mu\text{m}$  in radii with a flow dissipation rate  $400 \text{ cm}^2/\text{s}^3$ . In this case,  $dt_{\text{part}}$  is normalized by the response time of the 10  $\mu\text{m}$  water droplets, and the results are shown in Fig. 4b. Again,  $dt_{\text{flow}}$  is larger than  $dt_{\text{part}}$ , thus  $dt = dt_{\text{part}}$ . We also show results for the base case when the background turbulence was deactivated. Similar to the monodisperse case, an upper limit of  $dt_{\text{part}} = 0.15 \min(\tau_{p_1}, \tau_{p_2})$  is found for both the turbulence case and the base case.

It is interesting to note that for the monodisperse case the simulated collision kernel increases with  $dt$  if the  $dt$  is too large. This implies that the hydrodynamic interactions were underestimated when  $dt$  is large. This may be explained by the less frequent updates of the disturbance flows for a fixed total time interval, making the coupling between approaching droplets less effective in altering the droplet motion.

On the other hand, for the bidisperse system, the collision rate is slightly reduced for large  $dt$ . For this specific case, the trajectory of the smaller droplet is not accurately computed for a large  $dt$ . At every time step, any small disturbance flow (even if underestimated) experienced by the smaller droplet will push the droplet away from the larger droplet, thus reducing the collision count.

#### 4.2. Truncation radius $H$

The truncation radius  $H$  is determined by optimizing the balance between numerical accuracy and computational efficiency. We can reach higher computational efficiency by using a small truncation radius as it reduces the number of pairs in hydrodynamic-interaction considerations. However, a small radius may affect the accuracy of the calculated disturbance flow velocities. We performed a sensitivity analysis on the truncation radius  $H(=d^{(mk)}/a^{(m)})$  to determine the smallest hydrodynamic radius of influence without compromising the results.

Fig. 5 shows the results of the similar cases as shown in Section 4.1. It plots actual collision kernel normalized by the collision kernel obtained in the previous section using  $dt_{\text{part}} = 0.05\tau_p$  and a large nondimensional truncation radius  $H = 50$ . The data at  $d^{(mk)}/a^{(m)} = 0$  represent the geometric kernels or the limiting case when the hydrodynamic interactions are completely ignored. Again, the error bars show statistical uncertainties ( $\pm$ one standard deviation).

The results are insensitive to  $H$  if  $H \geq 30$  for both the monodisperse case and bidisperse cases, showing that the methodology can provide a self-consistent treatment to many-body interactions of a turbulent suspension. Fig. 5a also implies that the collision efficiency for the monodisperse case is slightly larger than one, namely, including hydrodynamic interactions leads to more collisions for a monodisperse system. Fig. 5b yields a collision efficiency of about 0.44 ( $=1/2.27$ ) for the turbulent flow case and about 0.38

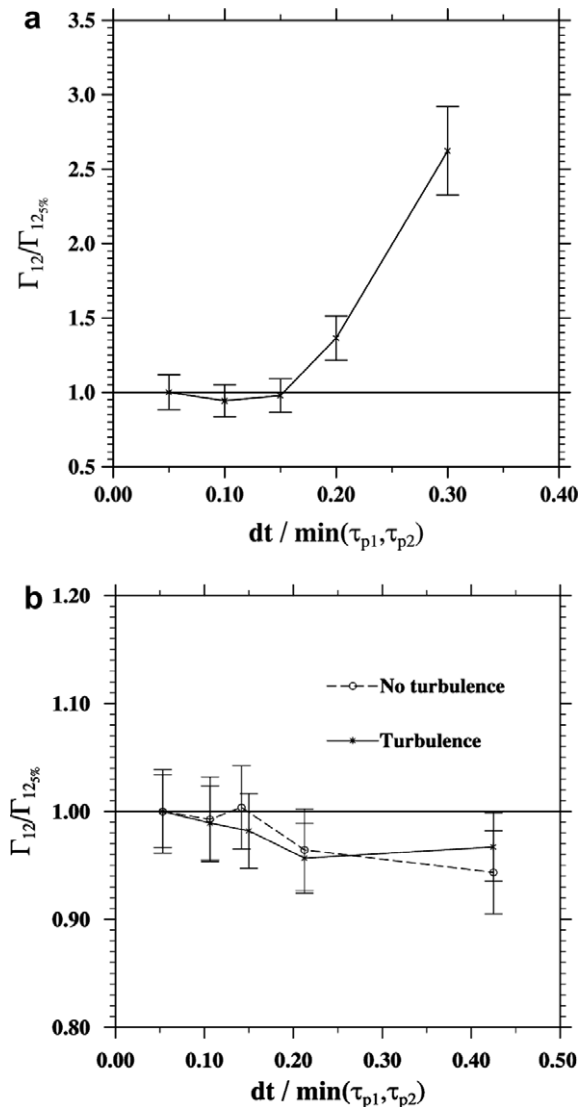


Fig. 4. Sensitivity analysis on the time step  $dt$ . (a) Monodisperse case. (b) Bidisperse case.

( $=1/2.66$ ) for the base case. It appears that for the turbulent collision case in Fig. 5b the critical  $H$  can be lower (about 20). This may be explained by the enhanced relative motion in a turbulent field, causing the hydrodynamic interaction effects to be more dominated by short-separation interactions. This is actually desirable for numerical treatment of hydrodynamic interactions. We speculate that the more vigorous the turbulence is, the more accurate the hydrodynamic interactions can be treated for a given  $H$ . A general rule of thumb according to the above results is that  $H = 30$  would be an optimum choice for numerical accuracy and computational efficiency.

For hydrodynamic interactions between two isolated particles in a stagnant fluid, other authors have previously proposed or adopted different values for the truncation radius. For instance, Lin and Lee [36] used in their study a value of 54 based on drag coefficient estimations. Cataneo and Semonia [57] in their experimental set up for equal-sized water droplets in the size range of 115  $\mu\text{m}$  to 700  $\mu\text{m}$  in diameter, found the hydrodynamic interactions remain important at distances larger or equal to 100 diameters. The water droplets used by Cataneo and Semonia [57], because of the larger size, can generate long wakes that can disturb the background field over a large distance. In our work, we consider only Stokes disturbance flows. For most production runs,

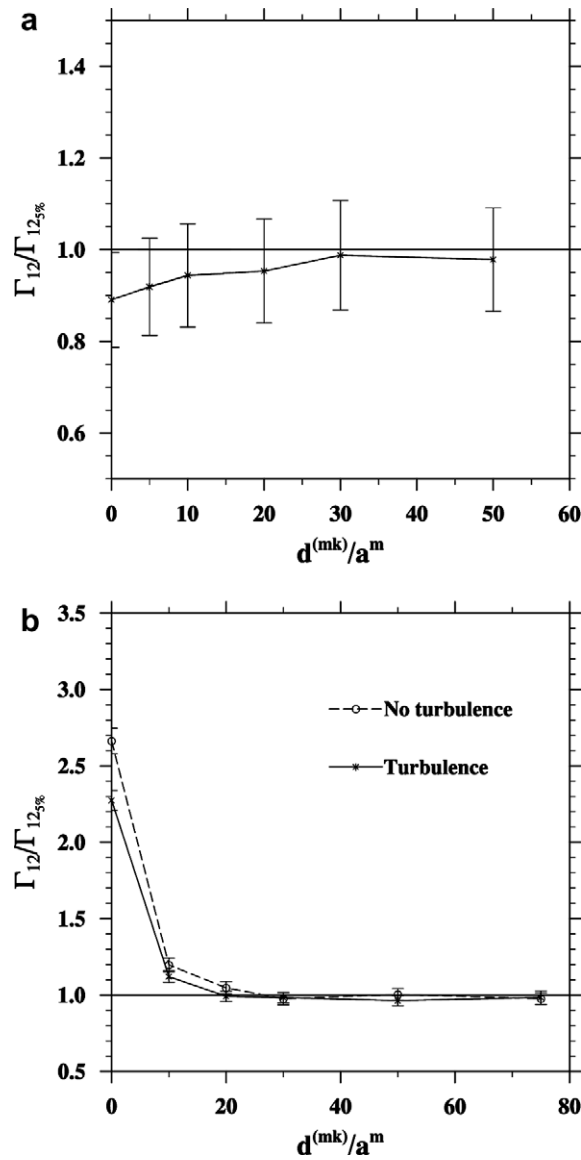


Fig. 5. Sensitivity analysis on normalized truncation radius. (a) Monodisperse case. (b) Bidisperse case.

we used a value of  $H = 50$ , larger than the optimum value obtained based on the two tests to ensure numerical accuracy for other parameter settings while keeping the computational cost manageable.

#### 4.3. Convergence test for the Gauss–Seidel procedure

Recall that the large linear system of dimension  $3N_p$  for  $\mathbf{u}^{(k)}$  is solved by the Gauss–Seidel procedure. The convergence condition was that the normalized difference between the current iteration and the previous iteration be within a certain tolerance  $\varepsilon$ . The selection of  $\varepsilon$  is then important as a small  $\varepsilon$  implies more iterations and larger computational effort, while a large  $\varepsilon$  may affect the accuracy of the results. We typically chose  $\varepsilon = 10^{-5}$ . This tolerance was also used in the previous subsections. Fig. 6 shows that the number of iterations depends on the number of particles (or equivalent the number of particle pairs). As expected, a larger number of particles requires more iterations to reach convergence as the dimension of the system is larger. Furthermore, the monodisperse case required more iterations than the bidisperse cases as the particle radius was

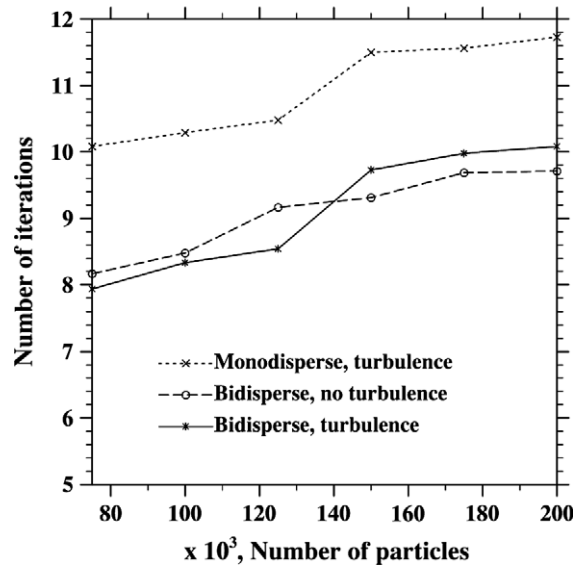


Fig. 6. Dependence of number of iterations on number of particles in the system.

larger, thus, the actual hydrodynamic radius of influence was larger. Therefore, the number of iterations depends on the number of particles and particle size. The number of iterations for both bidisperse cases are similar, thus, the background turbulence has little influence on the number of iterations.

Fig. 7 shows how the normalized errors for each disturbance velocity components, as defined in Eq. (14) vary with the number of iterations for a specific particle at a specific time step. The normalized errors decrease monotonically, indicating that the iterative method works well. From the plots, the selected criterion ( $\varepsilon = 10^{-5}$ ) is satisfied at the fourth iteration on all velocity components for both cases. The bidisperse case without turbulence is not shown as it presented similar trend as the bidisperse case with turbulence. The number of iterations also grows with increasing truncation radius as the number of pairs participating in hydrodynamic interactions is increased.

#### 4.4. Statistical uncertainties and their dependence on $N_p$

For a given simulation time and computational domain size, the number of particles determines the number of pairs and the total collision rate. A larger number of particles lead to a larger number of collisions and smaller statistical errors. Warshaw [58] showed that the number of collisions between two groups of particles in a time interval  $T$  is binomially distributed, with a mean equal to  $n_{\text{pairs}}\Gamma T/\Omega$  readily found from Eq. (15) and a variance of  $n_{\text{pairs}}\Gamma T/\Omega(1 - \Gamma T/\Omega)$ . Thus, the ratio of the standard deviation to the mean value (relative uncertainty) is given by

$$\text{Relative uncertainty for computed } \Gamma = \left( \frac{\frac{\Omega}{\Gamma T} - 1}{n_{\text{pairs}}} \right)^{1/2}. \quad (16)$$

This equation shows that the relative uncertainty depends on the time duration  $T$  of the numerical experiment, the computational-domain volume  $\Omega$  and the collision kernel  $\Gamma$  itself, and the number of particle pairs ( $n_{\text{pairs}}$ ).  $n_{\text{pairs}} = N_p(N_p - 1)/2$  for a monodisperse system and  $n_{\text{pairs}} = N_{p1}N_{p2}$  for a bidisperse system. The volume  $\Omega$  is fixed in the DNS simulations. The relative uncertainty may be further reduced by averaging over several independent runs of same parameter setting but different initial flow or particle realizations.

For a production run,  $\Omega$  and  $T$  are known in advance and  $\Gamma$  can be estimated during the simulation. If the total concentration of particles is not limited by the physical problem, the number of particles ( $N_p$  or  $N_{p1}$  and  $N_{p2}$ ) may be varied to obtain a required statistical uncertainty, as long as the dilute condition is maintained. In the context of cloud physics, the dilute condition can easily be maintained since the droplet

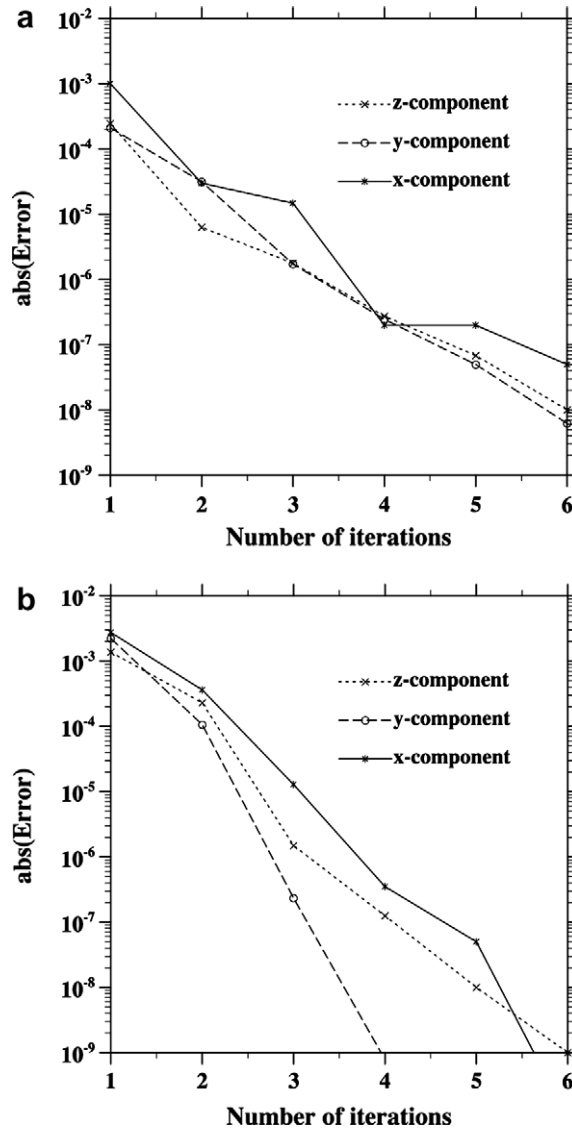


Fig. 7. Normalized errors as a function of number of iterations during a specific time step and for a specific particle. (a) Monodisperse case. (b) Bidisperse case in turbulence flow.

size and volume fraction are so small, even if the number concentration is made 10 times larger than what is observed in clouds.

Fig. 8 shows a comparison of the predicted relative uncertainty with the calculated relative uncertainty for both the monodisperse case and bidisperse case used above. The agreement between theory and the data is excellent. A total of 200,000 particles ( $N_p = 200,000$  or  $N_{p1} = N_{p2} = 100,000$ ) were used for the runs shown in Fig. 8.

### 5. Code validation and computational tests

In this section, we perform test runs to validate the implementation and show capabilities of the approach. We also report on the computational speed of the code and the distribution of computational time over different tasks.

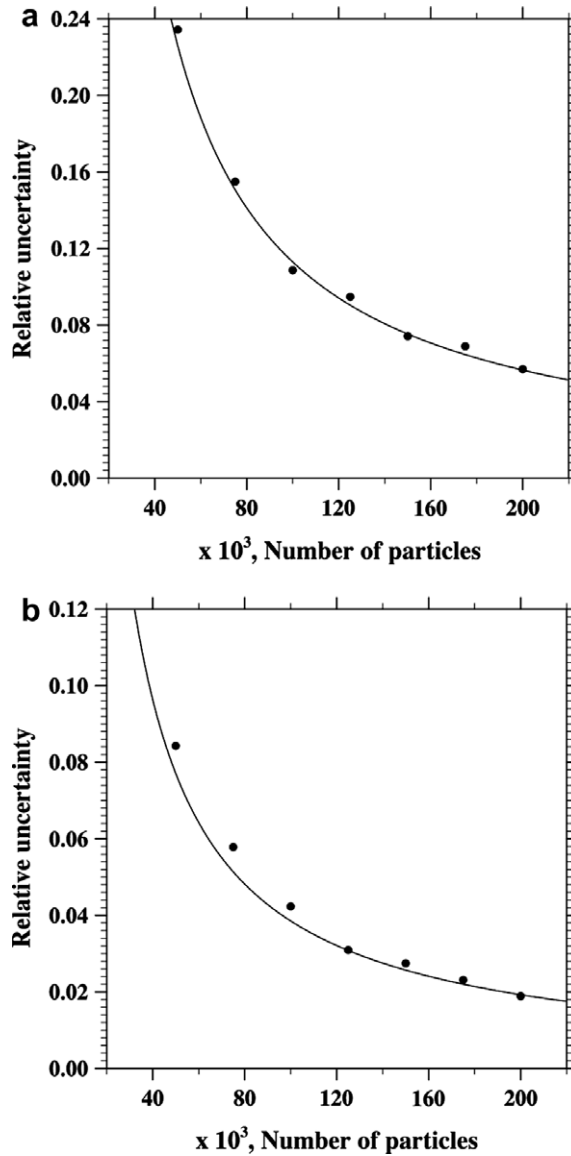


Fig. 8. Relative uncertainty vs. number of particles. (a) Monodisperse case. (b) Bidisperse case. Solid line is based on the theory, Eq. (16). Dots are from numerical experiments.

### 5.1. Validation test

Many authors have studied the hydrodynamic interaction effects on the collisions of two isolated particles settling in a stagnant fluid [34,36,59,60]. This can be viewed as a special case in our approach and thus can be used as a consistency validation test for our code implementation.

The parameter used to measure the hydrodynamic interaction effects on the collision of two particles is the collision efficiency  $E_{12}$ . For the case of two isolated particles settling in a stagnant fluid,  $E_{12}$  can be computed as [1]

$$E_{12} = \frac{y_c^2}{R^2}, \quad (17)$$

where the geometric collision radius  $R$  is the sum of the radii of two colliding particles,  $R = a_1 + a_2$ ;  $y_c$  is the far-field, off-center horizontal separation of the grazing trajectory of the smaller particle relative to the larger

particle. As a result of hydrodynamic interactions,  $y_c$  is smaller than  $R$ . In our general approach, a large number of particles are simultaneously considered with many-body interactions,  $E_{12}$  is then the ratio of number of collisions with hydrodynamic interactions to the number of collisions when the hydrodynamic interactions are completely ignored

$$E_{12} = \frac{\text{Number of collisions with HI}}{\text{Number of collisions without HI}}. \quad (18)$$

To obtain the collision efficiency based on Eq. (17), we developed a test code similar to previous studies of Klett and Davis [60] and Lin and Lee [36]. The trajectories of two particles falling under gravity in a stagnant fluid are numerically integrated. The initial far-field off-center horizontal separations was varied until the grazing trajectory was found. The hydrodynamic interactions between the particle pair were modeled using the same improved superposition method [38].

Fig. 9 shows the results from the two different approaches. The solid line represents  $E_{12}$  obtained using Eq. (17), while the dots are numerical results using our general approach. In this test, the large particle is a water droplet of  $a_1 = 25 \mu\text{m}$  in radius. In our general code, turbulence was deactivated to allow the droplets to settle under gravity and hydrodynamic interactions only. Four different cases with  $a_2/a_1 = 0.2, 0.4, 0.6,$  and  $0.8$  were performed. An excellent agreement is observed between the general approach and the simple approach. This is expected as the volume concentration of particles is very low ( $\sim 10^{-6}$ ) so two-particle interactions dominate hydrodynamic interactions in the system.

Fig. 10 illustrates the hydrodynamic interactions between two particles using our hybrid DNS approach for identical parameter setting but with the background turbulence switched off and on. Here the three trajectories of the smaller particles relative to the large particles were selected with a minimum separation distance less than 1% of the collision radius. They can be viewed as relative grazing trajectories. An important observation

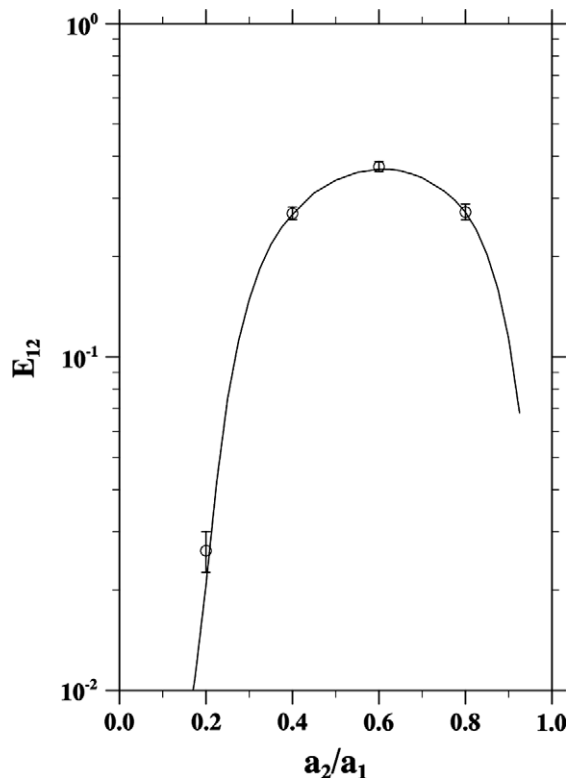


Fig. 9. A benchmark problem typically used in cloud physics community to measure hydrodynamic interaction effects. The larger particle in the test is a water droplet of  $a_1 = 25 \mu\text{m}$ . The fluid is stagnant. The solid line represents collision efficiency  $E_{12}$  obtained using Eq. (17). The dots are numerical results based on Eq. (18) using our general approach.

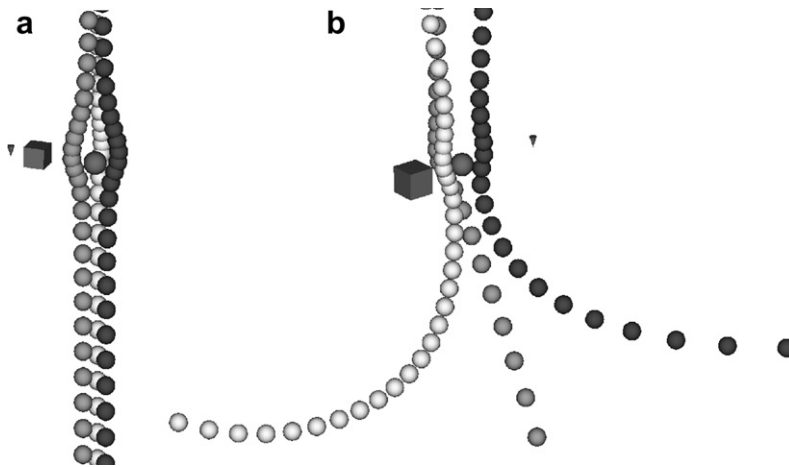


Fig. 10. Three grazing trajectories of 20 μm water droplet relative to 25 μm water droplet. (a) without turbulence, (b) turbulence at  $\epsilon = 400 \text{ cm}^2/\text{s}^3$ . The time interval for visualization was set to about 42% the inertial response time of the 20 μm droplet. The small cube in (a) has edge length equal to collision radius, while the small cube in (b) has edge length equal to 10% flow Kolmogorov length scale. The small cone indicates the direction of gravity.

is that while the relative motion is nearly vertical when there is no turbulence, the trajectories are strongly curved for the turbulent flow case. In all cases the trajectories become curved when the small particle is at a close proximity of the larger particle, due to the hydrodynamic interactions. Fig. 10b shows that our approach captures both the effects of the background turbulence and hydrodynamic interactions on the relative motion of droplets.

5.2. Computational speed

The hybrid DNS code was run on a parallel supercomputer SGI Origin 3800 at NCAR. The code was parallelized using OpenMP. The main parallelization efforts included the following tasks:

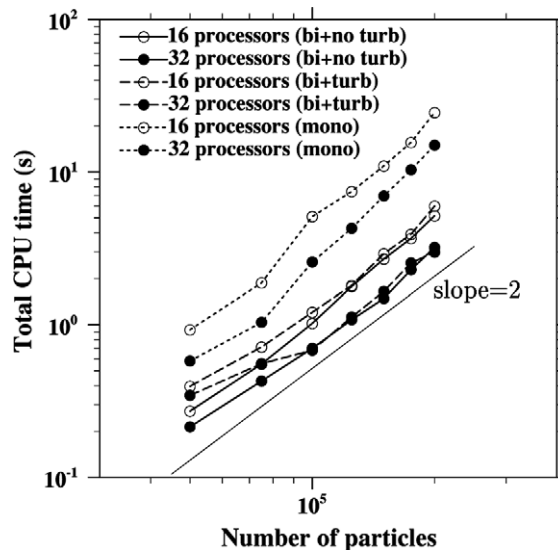


Fig. 11. Total CPU time spend per time step for the different test cases using 16 and 32 parallel processors.

- (1) Specify all large arrays as dynamically allocatable to reduce the stack size.
- (2) Optimize do-loops sequence. In the case of nested do-loops, the larger loop is placed as the outer loop in order to prepare it for the OpenMP implementation.
- (3) Parallelize do-loops by inserting OpenMP directives before and after the loops. Care was taken when identifying private variables in the OpenMP directives to ensure correct results.
- (4) Use an efficient parallel approach for the Fast Fourier Transform (FFT) as the flow simulation involves 9 FFTs per time step. A 3D FFT calculation of a  $N^3$  matrix can be accomplished by performing  $N$  local 2D FFTs and  $N^2$  1D FFTs. We divided the computational work evenly among all the  $N_{\text{proc}}$  processors, first giving each of them  $N/N_{\text{proc}}$  2D FFTs, and then  $N^2/N_{\text{proc}}$  1D FFTs. The FFT parallelization method follows the study of Dmitruk et al. [61].

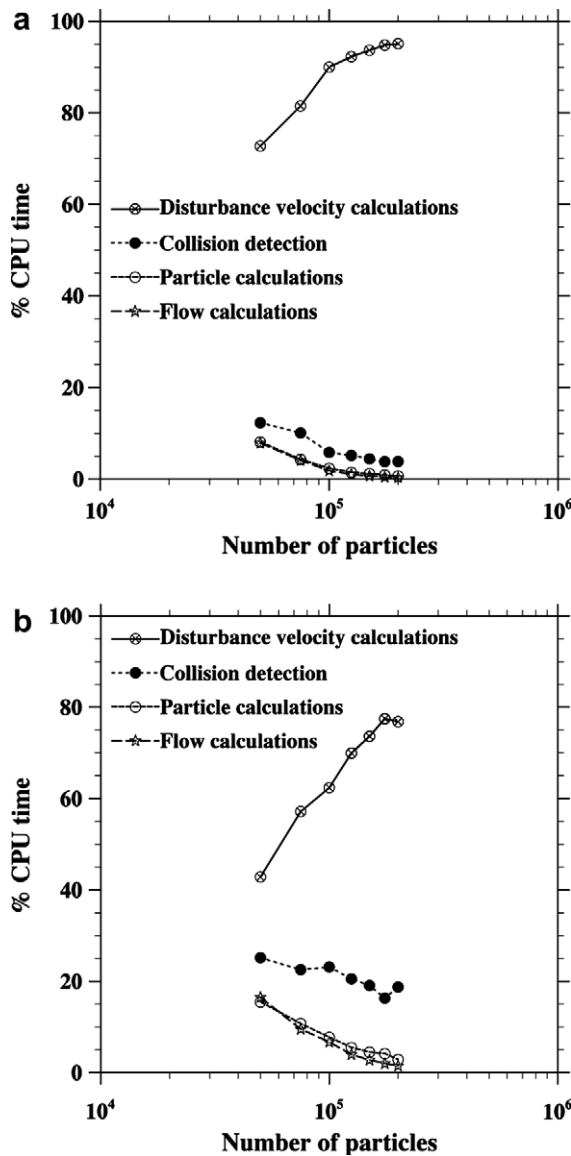


Fig. 12. CPU time percentage of the total time used by each of the four computational tasks. (a) Monodisperse case using 32 processors, (b) Bidisperse case in turbulent flow using 32 processors. The bidisperse case with no turbulent flow is not shown as it presented same trend as figure (b).

- (5) Apply an efficient FFT algorithm. For the local 2D and 1D FFTs in each processor we adopted the publicly available FFTW (<http://www.fftw.org>) by Frigo and Johnson which performed better than the in-house FFT algorithm on the SGI Origin 3800.

Typically, we used 16–32 processors. Fig. 11 shows the total CPU (wall-clock) time per time step for several different cases. The CPU time scales reasonably well with the number of processors used. The CPU time on flow evolution is a small fraction of the total time, due to the large number of particles used, and therefore, the total CPU time scales roughly as  $N_p^2$ .

The total computational time during a single time step can be decomposed according to the different computational tasks. The four main tasks are:

- (1) Advance the undisturbed fluid turbulence field using a pseudo-spectral method (flow calculation time  $t_{\text{flow}}$ ).
- (2) Interpolate the undisturbed fluid velocities at particle locations and advance the motion of all droplets (particle advancing time  $t_{\text{particle}}$ ).
- (3) Solve the disturbance flow velocities with Gauss–Seidel procedure (disturbance velocity calculation time  $t_{\text{disturbance}}$ ).
- (4) Detect collisions and compute pair kinematic and dynamic properties (collision detection time  $t_{\text{collision}}$ ).

Fig. 12 shows the fraction of the total time taken by each task. Clearly, the disturbance velocity calculation is the most time-consuming task. For most cases the disturbance velocity calculation resulting from hydrodynamic interactions takes 50% or more of the total CPU time. For the monodisperse case the percentage is even higher due to larger number of iterations in the Gauss–Seidel procedure. The next time-consuming task is the collision detection, taking roughly 10–20%. In Fig. 12 only results with 32 processors are shown as the results for 16 processors are similar.

Fig. 13 shows the actual CPU times for the four tasks, for the bidisperse case with turbulence using 16 processors. This figure illustrates the scaling of each computational time with the number of particles. The CPU time for flow evolution does not depend on number of particles. The CPU time for particle calculation scales as  $N_p$ . Finally, the collision detection and disturbance velocity calculation require a time proportional to  $N_p^2$ .

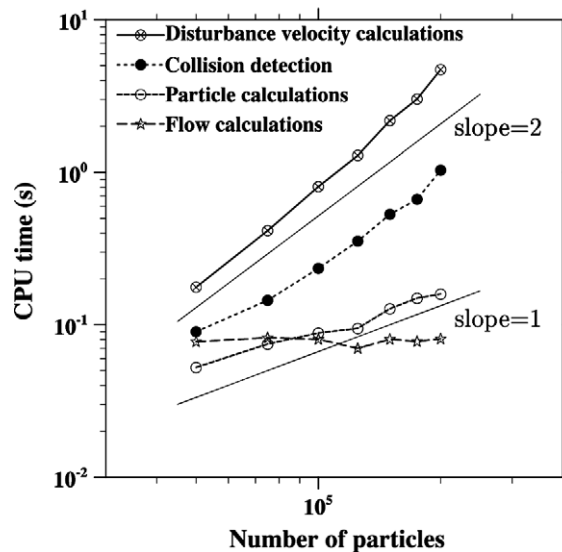


Fig. 13. Actual CPU times for the different computational tasks for the bidisperse case in turbulence using 16 processors.

## 6. Summary and concluding remarks

A hybrid direct numerical simulation method was proposed for turbulent collisions of hydrodynamically-interacting particles. The method consists of direct simulation of an undisturbed turbulent flow, generated and maintained at large scales, and an analytical representation of local small-scale disturbance flows induced by the presence of particles. The no-slip boundary condition on each particle was satisfied when averaged over the surface of the particle [38]. The approach assumes that: (1) the disturbance flow is very localized in space due to the dominant viscous effect; (2) there is a sufficient separation of length scales, namely, the particle size is much less than the smallest length scale (i.e., Kolmogorov length) of the undisturbed flow. The hybrid DNS approach, although very preliminary in nature, represents the most advanced approach available for treating turbulent collision of hydrodynamically-interacting particles [6]. It has also been used to understand, in a turbulent flow, the enhanced settling of particles due to hydrodynamic interactions [67], a phenomenon observed experimentally by Aliseda et al. [7].

In this study, we considered several implementation issues to ensure numerical accuracy and consistency of the approach, including the determination of time step size, the hydrodynamic interaction radius, and iterative method for the disturbance velocities. Guidelines have been developed for the time step size and the hydrodynamic interaction radius. Statistical uncertainties in the system were also briefly discussed, showing that a simple theory based on Warshaw [58] provides a useful estimate of the uncertainties on the collision rates.

It was found that the most time-consuming part of the approach is the solution of disturbance flow velocities due to the large number of particles involved. It is desired to improve the computational speed for this part of the approach in the future. In this regard, ideas from recent developments in accelerated Stokesian dynamics simulations [40–43] could be adapted for our purpose in handling the many-body problem encountered in computing the disturbance flow velocities. The idea would be to use a wave-space representation and fast Fourier transform to treat long-range many-body interactions.

As was pointed out in Section 1, the method shown here represents a first step towards a rigorous modeling of a three-way coupling system. Here, we comment on future directions to further develop the hybrid DNS approach. First, the hydrodynamic interaction radius needs to be formulated in terms of a more realistic representation of the far-field disturbance flow with a consideration of fluid inertial effects in both the disturbance flow and the background turbulence. This would eliminate the need to adjust  $H$  in our approach. Second, the improved superposition method does not correctly model the lubrication force between two particles, as pointed out in Wang et al. [38]. Analytical methods using multipole techniques at large separations and lubrication expansion for small separations [62–64] are the logical next step to improve our approach. Finally, when the minimum separation between two particles approaches the mean free path of fluid medium, non-continuum effects [65,66] will have to be included.

## Acknowledgements

This study has been supported by the National Science Foundation through Grants ATM-0114100 and ATM-0527140, and by the National Center for Atmospheric Research (NCAR). NCAR is sponsored by National Science Foundation. The support of NCAR Faculty Fellowship to L.P.W. is gratefully acknowledged. Most of the simulations were conducted using SGI Origin 3800/2100 at NCAR. O.A. is grateful to the additional computing resources provided by the Scientific Computing Division at NCAR. We also thank Dr. Bogdan Rosa for his comments on the paper.

## References

- [1] H.R. Pruppacher, J.D. Klett, *Microphysics of Clouds and Precipitation*, Klumer Academic Publishers, AH Dordrecht, The Netherlands, 1997.
- [2] J.H. Seinfeld, S.N. Pandis, *Atmospheric Chemistry and Physics: From Air Pollution to Climate Change*, Wiley, 1997.
- [3] S. Sundaram, L.R. Collins, Collision statistics in an isotropic, particle-laden turbulent suspension, *J. Fluid Mech.* 335 (1997) 75–109.
- [4] L.P. Wang, A. Wexler, Y. Zhou, Statistical mechanical description and modelling of turbulent collision of inertial particles, *J. Fluid Mech.* 415 (2000) 117–153.
- [5] Y. Zhou, A. Wexler, L.-P. Wang, Modelling turbulent collision of bidisperse inertial particles, *J. Fluid Mech.* 433 (2001) 77–104.

- [6] L.P. Wang, O. Ayala, S.E. Kasprzak, W.W. Grabowski, Theoretical formulation of collision rate and collision efficiency of hydrodynamically-interacting cloud droplets in turbulent atmosphere, *J. Atmos. Sci.* 62 (2005) 2433–2450.
- [7] A. Aliseda, A. Cartellier, F. Hainaux, J.C. Lasheras, Effect of preferential concentration on the settling velocity of heavy particles in homogeneous isotropic turbulence, *J. Fluid Mech.* 468 (2002) 77–105.
- [8] G.K. Batchelor, Sedimentation in a dilute dispersion of spheres, *J. Fluid Mech.* 52 (1972) 245–268.
- [9] G.K. Batchelor, Sedimentation in a dilute polydisperse system of interacting spheres. Part 1. General theory, *J. Fluid Mech.* 119 (1982) 379–408.
- [10] E.J. Hinch, Sedimentation of small particles, in: E. Guyon, J.-P. Nadal, Y. Pomeau (Eds.), *Disorder and Mixing*, Kluwer Academic Publishers, 1988, pp. 153–161.
- [11] S. Kim, S.J. Karrila, *Microhydrodynamics, Principles and Selected Applications*, Butterworth-Heinemann, Boston, 1991, 507pp.
- [12] H. Nicolai, B. Herzhaft, E.J. Hinch, L. Oger, E. Guazzelli, Particle velocity fluctuations and hydrodynamic self-diffusion of sedimenting non-Brownian spheres, *Phys. Fluids* 7 (1995) 12–23.
- [13] R.H. Davis, Hydrodynamic diffusion of suspended particles: a symposium, *J. Fluid Mech.* 310 (1996) 325–335.
- [14] S. Ramaswamy, Issues in the statistical mechanics of steady sedimentation, *Adv. Phys.* 50 (2001) 297–341.
- [15] V. Kumaran, D.L. Koch, Properties of a bidisperse particle gas suspension. 1. Collision time small compared with viscous relaxation time, *J. Fluid Mech.* 247 (1993) 623–641.
- [16] V. Kumaran, D.L. Koch, Properties of a bidisperse particle gas suspension. 2. Viscous relaxation time small compared with collision time, *J. Fluid Mech.* 247 (1993) 643–660.
- [17] B.K. Brunk, D.L. Koch, L.W. Lion, Turbulent coagulation of colloidal particles, *J. Fluid Mech.* 364 (1998) 81–113.
- [18] M.B. Pinsky, A.P. Khain, Turbulence effects on droplet growth and size distribution in clouds – A review, *J. Aerosol Sci.* 28 (1997) 1177–1214.
- [19] P.A. Vaillancourt, M.K. Yau, Review of particle–turbulence interactions and consequences for cloud physics, *Bull. Am. Meteor. Soc.* 81 (2000) 285–298.
- [20] R.A. Shaw, Particle–turbulence interactions in atmospheric clouds, *Annu. Rev. Fluid Mech.* 35 (2003) 183–227.
- [21] Y. Pan, S. Banerjee, Numerical simulation of particle interactions with wall turbulence, *Phys. Fluids* 8 (1996) 2733–2755.
- [22] Y. Pan, S. Banerjee, Numerical investigation of the effects of large particles on wall-turbulence, *Phys. Fluids* 9 (1997) 3786–3807.
- [23] M.R. Maxey, B.K. Patel, Localized force representation for particles sedimenting in Stokes flow, *Int. J. Multiphase Flow* 27 (2001) 1603–1626.
- [24] S. L. Dance, M.R. Maxey, Incorporation of lubrication effects into the force-coupling method for particulate two-phase flow, *J. Comp. Phys.* 189 (2003) 212–238.
- [25] A. Prosperetti, H.N. Oguz, A new (o)(N) method for the numerical simulation of dispersed systems: Potential flow of spheres, *J. Comput. Phys.* 167 (2001) 196–216.
- [26] S. Takagi, H.N. Oguz, Z. Zhang, A. Prosperetti, PHYSALIS: a new method for particle simulation – Part II: two-dimensional Navier–Stokes flow around cylinders, *J. Comput. Phys.* 187 (2003) 371–390.
- [27] T. Tsuji, R. Narutomi, T. Yokomine, S. Ebara, A. Shimizu, Unsteady three-dimensional simulation of interactions between flow and two particles, *Int. J. Multiphase Flow* 29 (2003) 1431–1450.
- [28] H.H. Hu, Direct simulation of flows of solid-liquid mixtures, *Int. J. Multiphase Flow* 22 (1996) 332–335.
- [29] A.A. Johnson, T.E. Tezduyar, Simulation of multiple spheres in a liquid-filled tube, *Comput. Methods Appl. Mech. Eng.* 134 (1996) 351–373.
- [30] A.J.C. Ladd, Numerical simulations of particulate suspensions via a discretized Boltzmann equation. Part 1. Theoretical foundation, *J. Fluid Mech.* 271 (1994) 285–309.
- [31] Z.G. Feng, E.E. Michaelides, The immersed boundary-lattice Boltzmann method for solving fluid-particles interaction problems, *J. Comput. Phys.* 195 (2004) 602–628.
- [32] A. Ten Cate, J.J. Derksen, L.M. Portela, H.E.A. van der Akker, Fully resolved simulations of colliding monodisperse spheres in forced isotropic turbulence, *J. Fluid Mech.* 519 (2004) 233–271.
- [33] I. Langmuir, The production of rain by a chain reaction in cumulus clouds at temperature above freezing, *J. Meteorol.* 5 (1948) 175–192.
- [34] U. Shafirir, M. Neiburger, Collision efficiencies of two spheres falling in a viscous medium, *J. Geophys. Res.* 68 (1963) 4141–4147.
- [35] K.V. Beard, S.N. Grover, Numerical collision efficiencies for small raindrops colliding with micron size particles, *J. Atmos. Sci.* 31 (1974) 543–550.
- [36] C. Lin, S. Lee, Collision efficiency of water drops in the atmosphere, *J. Atmos. Sci.* 32 (1975) 1412–1418.
- [37] M. Pinsky, A. Khain, M. Shapiro, Collisions of small drops in a turbulent flow. Part I. Collision efficiency. Problem formulation and preliminary results, *J. Atmos. Sci.* 56 (15) (1999) 2585–2600.
- [38] L.P. Wang, O. Ayala, W.W. Grabowski, On improved formulations of the superposition method, *J. Atmos. Sci.* 62 (2005) 1255–1266.
- [39] J.F. Brady, G. Bossis, Stokesian dynamics, *Annu. Rev. Fluid Mech.* 20 (1988) 111–157.
- [40] A.S. Sangani, G.B. Mo, An O(N) algorithm for Stokes and Laplace interactions of particles, *Phys. Fluid* 8 (1996) 1990–2010.
- [41] K. Ichiki, J.F. Brady, Many-body effects and matrix inversion in low Reynolds number hydrodynamics, *Phys. Fluids* 13 (2001) 350–353.
- [42] A. Sierou, J.F. Brady, Accelerated Stokesian dynamics simulations, *J. Fluid Mech.* 448 (2001) 115–146.
- [43] K. Ichiki, Improvement of the Stokesian dynamics method for systems with a finite number of particles, *J. Fluid Mech.* 452 (2002) 231–262.
- [44] P. Moin, K. Mahesh, Direct numerical simulation: a tool in turbulence research, *Annu. Rev. Fluid Mech.* 30 (1998) 539–578.

- [45] C.L. Lin, S.C. Lee, The effect of vertical separation on droplet collision efficiency Reply to comments by Cataneo and Semonin, *J. Atmos. Sci.* 33 (1976) 1826–1827.
- [46] L.P. Wang, M.R. Maxey, Settling velocity and concentration distribution of heavy particles in homogeneous isotropic turbulence, *J. Fluid Mech.* 256 (1993) 27–68.
- [47] K. Hu, R. Mei, Effect of inertia on the particle collision coefficient in Gaussian turbulence, in: *CDROM Proceedings, ASME Fluid Engineering Div. Summer Meeting, 1997*.
- [48] S. Balachandar, M.R. Maxey, Methods for evaluating fluid velocities in spectral simulations of turbulence, *J. Comput. Phys.* 83 (1989) 96–125.
- [49] K.E. Atkinson, *An Introduction to Numerical Analysis*, John Wiley and Sons, New York, 1978, 587pp.
- [50] Y. Noh, H.J.S. Fernando, The transition in the sedimentation pattern of a particle cloud, *Phys. Fluids*, 5 (1993) 3049–3055.
- [51] D.L. Koch, E.S.G. Shaqfeh, Screening in sedimenting suspensions, *J. Fluid Mech.* 224 (1991) 275–303.
- [52] A.J.C. Ladd, Hydrodynamic screening in sedimenting suspensions of non-Brownian spheres, *Phys. Rev. Lett.* 76 (1996) 1392–1395.
- [53] M.P. Brenner, Screening mechanisms in sedimentation, *Phys. Fluids* 11 (1999) 754–772.
- [54] M.P. Allen, D.J. Tildesley, *Computer Simulation of Liquids*, Oxford University Press, 1989.
- [55] Y. Zhou, A. Wexler, L.-P. Wang, On the collision rate of small particles in isotropic turbulence. II. Finite inertia case, *Phys. Fluids* 10 (1998) 1206–1216.
- [56] E. Eswaran, S.B. Pope, An examination of forcing in direct numerical simulations of turbulence, *Comp. Fluids* 16 (1988) 257–278.
- [57] R. Cataneo, R.G. Semonin, Comments on “Collision efficiency of water drops in the atmosphere”, *J. Atmos. Sci.* 33 (1976) 1826.
- [58] M. Warshaw, Cloud droplet coalescence: statistical foundations and a one-dimensional sedimentation model, *J. Atmos. Sci.* 24 (1967) 278–286.
- [59] M.H. Davis, J.D. Sartor, Theoretical collision efficiencies for small cloud droplets in Stokes flow, *Nature* 215 (1967) 1371–1372.
- [60] J. Klett, M. Davis, Theoretical collision efficiencies of cloud droplets at small Reynolds numbers, *J. Atmos. Sci.* 30 (1973) 107–117.
- [61] P. Dmitruk, L.P. Wang, W.H. Matthaeus, R. Zhang, D. Seckel, Scalable parallel FFT for spectral simulations on a Beowulf cluster, *Parallel Comput.* 27 (2001) 1921–1936.
- [62] D.J. Jeffrey, Y. Onishi, Calculation of the resistance and mobility functions for two unequal rigid spheres in low-Reynolds-number flow, *J. Fluid Mech.* 139 (1984) 261–290.
- [63] R.H. Davis, The rate of coagulation of a dilute polydisperse system of sedimenting spheres, *J. Fluid Mech.* 145 (1984) 179–199.
- [64] J. Chun, D.L. Koch, Coagulation of monodisperse aerosol particles by isotropic turbulence, *Phys. Fluids* 17 (2005) 027102.
- [65] L.M. Hocking, Effect of slip on motion of a sphere close to a wall and of 2 adjacent spheres, *J. Eng. Math.* 7 (1973) 207–221.
- [66] R.R. Sundararakumar, D.L. Koch, Non-continuum lubrication flows between particles colliding in a gas, *J. Fluid Mech.* 313 (1996) 283–308.
- [67] L.P. Wang, O. Ayala, W.W. Grabowski, Effects of aerodynamic interactions on the motion of heavy particles in a bidisperse suspension, *J. Turbul.* (2006) submitted for publication.